



ELSEVIER

Fluid Dynamics Research 33 (2003) 403–431

FLUID DYNAMICS
RESEARCH

Enhanced stretching of material lines by antiparallel vortex pairs in turbulence

Susumu Goto*, Shigeo Kida

*Theory and Computer Simulation Center, National Institute for Fusion Science, 322-6 Oroshi-cho,
Toki 509-5292, Japan*

Received 23 November 2002; received in revised form 2 May 2003; accepted 6 May 2003

Communicated by M.-E. Brachet

Abstract

Deformations of material lines in homogeneous isotropic turbulence of an incompressible viscous fluid are numerically investigated to understand the physical mechanism of the enhanced stretching of material lines in turbulence. It is shown qualitatively by careful visualizations of numerical data and quantitatively by detailed numerical analysis that tubular vortical coherent structures in small scales of turbulence play crucial roles in such intensive stretching of material lines. In particular, the tubular vortices tend to align to each other in an antiparallel manner, and a pair of antiparallel vortices strongly stretch material lines in two regions around the hyperbolic stagnation points between them.

© 2003 Published by The Japan Society of Fluid Mechanics and Elsevier B.V. All rights reserved.

PACS: 47.27.-i; 47.52.+j

Keywords: Turbulence; Mixing; Stretching; Material line; Antiparallel vortices

1. Introduction

A line in a fluid which always consists of the same set of fluid particles is called a material line. It has been theoretically predicted (Batchelor, 1952) and numerically confirmed (Girimaji and Pope, 1990; Kida and Goto, 2002) that the total length of a material line increases exponentially in time in homogeneous isotropic turbulence. This intensive stretching of material lines (and surfaces as well) is believed to reflect a high potential of mixing by turbulence. Since turbulent mixing is one of the most challenging unsolved problems in fluid dynamics, the deformations and stretching

* Corresponding author. Tel.: +81-572-58-2561; fax: +81-572-58-2626.

E-mail addresses: goto@toki.theory.nifs.ac.jp (S. Goto), kida@toki.theory.nifs.ac.jp (S. Kida).

of material objects have been investigated by many authors to build a foothold for understanding of strong mixing. In spite of the long history, however, neither the physical mechanism of strong mixing nor that of exponential stretching of material objects has been understood as yet.

Batchelor (1952) also suggested the validity of Kolmogorov's (Kolmogorov, 1941) scaling law in material line statistics. That is, the statistics are characterized only by the Kolmogorov length $\eta = \varepsilon^{-1/4} \nu^{3/4}$ and the Kolmogorov time $\tau_\eta = \varepsilon^{-1/2} \nu^{1/2}$, where ε is the mean dissipation rate of energy per unit mass and ν is the kinematic viscosity. The Kolmogorov scaling in the material line statistics is verified numerically in Girimaji and Pope (1990) by the use of direct numerical simulation (DNS) of infinitesimal material line elements. Note however that the non-equivalence between the statistics of finite-size material objects and those of infinitesimal material elements has been shown recently (Goto and Kida, 2002). Nevertheless, as will be described in Section 3 of the present article, the true statistics¹ of finite-sized material lines also obey Kolmogorov's scaling law.

This Kolmogorov scaling of material objects may be reasonable because they are deformed and stretched by eddies on small length scales, i.e., scales around η . Kolmogorov-scale eddies were merely an abstract concept in the era of Batchelor, but now we know, from recent detailed DNS data analyses, their concrete properties. That is, they have tubular shapes with radius of $O(5\eta)$, circulation of $O(100\nu)$, and length ranging between $O(\eta)$ and the integral length (Makihara and Kida, 2003). It is rather surprising that the length of the small-scale eddies is much longer than the Kolmogorov length. We must bear in mind that only the cross-sectional structures of the small-scale eddies are in the Kolmogorov scales. It is readily shown that a solo tubular vortex has very weak ability to stretch material lines. More precisely, simple wrapping of a material line around a tubular vortex yields only algebraic stretching of the total length of the line. The main purpose of the present study is to show that not a single vortex but pairs of them produce effective stretching.

The rest of the present article is organized as follows. Governing equations and the numerical algorithm to solve them are described briefly in the next section. Numerically estimated statistics of material lines and tubular vortices are given in Sections 3 and 4, respectively. It will be shown that the statistics of both material lines and cross-sectional structures of tubular vortices obey Kolmogorov's scaling law. In Section 4, it is also shown that the vortices tend to align with each other in an antiparallel manner. The main section is Section 5, where the physical mechanism of exponential stretching of material lines is explained as being caused by antiparallel pairs of tubular vortices. Finally, a summary of the present results, a brief discussion on stretching of material surfaces and a discussion of the Kolmogorov similarity of material lines are given in Section 6.

2. Governing equations and numerical scheme

In order to investigate the physical mechanism of strong stretching of material lines in turbulence, we perform DNS of material lines to high precision. The governing equations of the system and the numerical algorithm used to solve them are summarized below.

¹In this article, we shall show that the statistics of material lines, which are sufficiently longer than the Kolmogorov length but are finite, obey Kolmogorov's scaling law. Such statistics may be different from those of infinitely long material lines. We shall discuss the differences between the two statistics in the last section.

By definition, any point \mathbf{x}_n on a material line is advected by the local velocity as

$$\frac{d}{dt} \mathbf{x}_n(t) = \mathbf{u}(\mathbf{x}_n(t), t). \quad (1)$$

Here, $\mathbf{u}(\mathbf{x}, t)$ is the velocity field of an incompressible viscous fluid, which is governed by the Navier–Stokes equation,

$$\left(\frac{\partial}{\partial t} + \mathbf{u}(\mathbf{x}, t) \cdot \nabla \right) \mathbf{u}(\mathbf{x}, t) = -\frac{1}{\rho} \nabla p(\mathbf{x}, t) + \nu \nabla^2 \mathbf{u}(\mathbf{x}, t) + \mathbf{f}(\mathbf{x}, t), \quad (2)$$

and the continuity equation,

$$\nabla \cdot \mathbf{u}(\mathbf{x}, t) = 0 \quad (3)$$

with periodic boundary conditions in all three orthogonal directions. Here, ρ , $p(\mathbf{x}, t)$ and $\mathbf{f}(\mathbf{x}, t)$ are the constant density, the pressure field and an external forcing, respectively.

The temporal evolution of $\mathbf{u}(\mathbf{x}, t)$ is simulated by integrating (2) and (3) numerically by the use of the 4th-order Runge–Kutta–Gill scheme. The spatial derivatives are evaluated by the Fourier spectral method, where the phase shift method is employed for dealiasing. The amplitudes of Fourier components of velocity in a low-wavenumber range, less than $\sqrt{8}$ say, are kept constant in time to realize a statistically stationary state. In the following we shall mainly discuss small-scale statistics of the turbulence, which are not affected by this artificial (effective) large-scale forcing. We report here several cases of different values of the Taylor-length Reynolds number,

$$R_\lambda(t) = \frac{U(t)\lambda(t)}{\nu} = \sqrt{\frac{20}{3\nu\varepsilon(t)}} \mathcal{E}(t) \quad (4)$$

ranging between 57 and 252 on the temporal average, for each of which we have used appropriate numbers N^3 of numerical grid points between 128^3 and 512^3 in order to guarantee numerical accuracy for small-scale motions. Here, $U(t)$, $\mathcal{E}(t) = \frac{3}{2}U(t)^2$ and $\lambda(t) = \sqrt{15\nu U(t)^2/\varepsilon(t)}$ are the root mean square of a single component of $\mathbf{u}(\mathbf{x}, t)$, the kinetic energy per unit mass and the Taylor length, respectively.

A material line is expressed numerically by a set of a number of advecting points, each position $\mathbf{x}_n(t)$ of which moves according to (1). The right-hand side of (1) is estimated by 4³-point Lagrangian interpolation of the velocity field $\mathbf{u}(\mathbf{x}, t)$ at the numerical grid points obtained by the numerical method described above, and the time integration is carried out by the 4th order Runge–Kutta scheme with time increment twice of that for the velocity field. In order to express a line smoothly by the set of advecting points, the distance between any two adjacent points must be kept short enough. Whenever the distance exceeds a threshold, 1.5 times the numerical grid width, we add a new advecting point at a position between the two points which is determined by the 4-point Lagrangian interpolation along the line. Since the length of the material line increases exponentially in time (see the next section), this interpolation is made at every time step.

3. Kolmogorov’s scaling law in material line statistics

The purpose of this section is to confirm that the statistics of material lines obey Kolmogorov’s scaling law by performing a sufficiently large number (J) of DNS of many (M) sample lines over

Table 1

Parameters of simulations reported in Section 3. Here, dt is the time increment for the integration of the velocity field, M is the number of simultaneously simulated material lines, J is the number of realizations, and T is the time period integrated in a single simulation in the unit of the Kolmogorov time τ_η and the energy-containing-scale time \mathcal{T}

Run	N^3	ν	dt	M	J	T
7A	128^3	5×10^{-3}	1×10^{-2}	2^{14}	20	$10 \approx 50\tau_\eta \approx 2.3\mathcal{T}$
7B	128^3	2.5×10^{-3}	1×10^{-2}	2^{14}	20	$8 \approx 57\tau_\eta \approx 1.8\mathcal{T}$
8C	256^3	1.25×10^{-3}	2.5×10^{-3}	2^{14}	20	$5 \approx 50\tau_\eta \approx 1.1\mathcal{T}$
9D	512^3	6.25×10^{-4}	1.25×10^{-3}	2^{12}	20	$2.5 \approx 34\tau_\eta \approx 0.5\mathcal{T}$
9E	512^3	3.125×10^{-4}	1.25×10^{-3}	2^{12}	20	$2 \approx 39\tau_\eta \approx 0.4\mathcal{T}$

Table 2

Statistics of numerical turbulence. Temporal averages and fluctuations are shown. Here, R_λ , \mathcal{E} , ε , τ_η , η and λ are the Taylor-length Reynolds number, the kinetic energy per unit mass, its dissipation rate, the Kolmogorov time, the Kolmogorov length, and the Taylor length, respectively

Run	R_λ	\mathcal{E}	ε	τ_η	η	$k_{\max}\eta$	λ
7A	$(5.65 \pm 0.23) \times 10$	0.544 ± 0.039	0.124 ± 0.013	$(2.02 \pm 0.10) \times 10^{-1}$	$(3.17 \pm 0.08) \times 10^{-2}$	1.91	0.469 ± 0.014
7B	$(8.31 \pm 0.30) \times 10$	0.573 ± 0.031	0.127 ± 0.011	$(1.41 \pm 0.06) \times 10^{-1}$	$(1.87 \pm 0.04) \times 10^{-2}$	1.12	0.336 ± 0.009
8C	$(1.21 \pm 0.06) \times 10^2$	0.586 ± 0.048	0.124 ± 0.015	$(1.01 \pm 0.06) \times 10^{-1}$	$(1.12 \pm 0.03) \times 10^{-2}$	1.35	0.243 ± 0.009
9D	$(1.75 \pm 0.08) \times 10^2$	0.585 ± 0.037	0.119 ± 0.012	$(7.26 \pm 0.36) \times 10^{-2}$	$(6.74 \pm 0.17) \times 10^{-3}$	1.62	0.175 ± 0.007
9E	$(2.52 \pm 0.10) \times 10^2$	0.601 ± 0.036	0.121 ± 0.011	$(5.09 \pm 0.22) \times 10^{-2}$	$(3.99 \pm 0.09) \times 10^{-3}$	0.96	0.125 ± 0.004

long times (T). Simulation parameters and statistics of numerical turbulence are given in Tables 1 and 2, respectively. A measure of numerical accuracy for the small-scale motions, $k_{\max}\eta$, is shown in Table 2. Here, $k_{\max}(=0.47N)$ is the maximum resolved wavenumber in the present DNS. The frequently employed condition $k_{\max}\eta > 1$ is satisfied except in the largest Reynolds number case (run 9E). The time increment dt , shown in Table 1, of numerical integration should be smaller than the sweeping time $1/(k_{\max}\mathcal{E}^{1/2})$ of the smallest structure of turbulence by the large-scale motions.

Before discussing the statistics of material lines, we describe the numerical method. In order to obtain accurate statistics of material objects in turbulence we must simulate finite-sized material objects instead of infinitesimal ones, though many authors have preferred the latter. In other words, the frequently used assumption by Batchelor (1952) that statistics of material lines/surfaces are the same as those of infinitesimal material line/surface elements in statistically stationary homogeneous turbulence is not valid in general (Goto and Kida, 2002). This may be understood as follows. According to Batchelor, we suppose that a material line is a set of material line elements, each of which has a length $\ell^{(i)}(t)$ shorter than the characteristic length scale of the deformed line, which will be shown to be $O(10\eta)$ (Section 3.3). Then the line average of a quantity g along a material line defined by a line integral can be approximated by

$$\langle g \rangle_{\text{line}} = \frac{\int g(t) d\ell}{\int d\ell} \approx \frac{\sum_{i=1}^I g^{(i)}(t) \ell^{(i)}(t)}{\sum_{i=1}^I \ell^{(i)}(t)}, \quad (5)$$

where I is the number of line elements. This is valid. However, Batchelor (1952) further assumed that this could be approximated by the line-element average,

$$\langle g \rangle_{\text{line-element}} = \frac{1}{I} \sum_{i=1}^I g^{(i)}(t) \quad (6)$$

in statistically stationary homogeneous turbulence because all the line elements would become statistically equivalent after a sufficiently long time. Since this assumption makes numerical and theoretical treatments of material lines drastically simple, it has been frequently used in the study of material objects in homogeneous turbulence. Note that the line average (5) can be rewritten as a ratio of two line-element averages,

$$\langle g \rangle_{\text{line}} = \frac{\langle g \ell \rangle_{\text{line-element}}}{\langle \ell \rangle_{\text{line-element}}}. \quad (7)$$

By comparing (6) and (7), we find that the line average and the line-element average are identical if $\ell^{(i)}(t)$ and $g^{(i)}(t)$ are statistically independent of each other. However, for an important case of the stretching rate, i.e. $g^{(i)} = \gamma_e^{(i)} \equiv d \log \ell^{(i)} / dt$, it can be shown (Goto and Kida, 2002; Kida and Goto, 2002) that the correlation between γ_e and ℓ never diminishes even at large times, and that $\langle \gamma_e(t) \rangle_{\text{line}} = 0.17\tau_\eta^{-1}$ is not identical to $\langle \gamma_e(t) \rangle_{\text{line-element}} = 0.13\tau_\eta^{-1}$ in turbulence at $R_\lambda = 58$. For this reason, we report here DNS results of finite-sized material lines.

3.1. Temporal evolution of material line

Material lines appear to evolve differently depending upon the observation scales. In Figs. 1 and 2, we show typical temporal evolutions of a single material line viewed on the energy-containing scale and the Kolmogorov scale, respectively. Three cases of different Reynolds numbers are compared. The left five panels show the results at $R_\lambda = 57.3$ (run 7A), the middle at 84.1 (run 7B), and the right at 122 (run 8C). Time elapses from top to bottom. A straight line is set at the initial time.

First, let us concentrate on Fig. 1. The time increment between two vertically successive panels is $0.2\mathcal{T}$, where $\mathcal{T} = \mathcal{E}/\varepsilon$ is an energy-containing-scale time (the so-called eddy-turnover time). The large box drawn in these figures is the whole computational domain, whose side length is about $2\mathcal{L}$, where $\mathcal{L} = \mathcal{E}^{3/2}/\varepsilon$ is a length² which characterizes energy-containing-scale motions, while the side of small boxes in each figure indicates 10η . A material line is deformed more rapidly into a more complicated structure at larger Reynolds numbers. Actually, the total length,

$$L(t) = \sum_{i=1}^{I(t)} \ell^{(i)}(t) \quad (\ell^{(i)}(t) = |\mathbf{l}^{(i)}(t)|) \quad (8)$$

of the material line increases more rapidly for larger Reynolds numbers in the energy-containing-scale time unit \mathcal{T} . Here, $\mathbf{l}^{(i)}(t) = \mathbf{x}_n^{(i+1)}(t) - \mathbf{x}_n^{(i)}(t)$ is the line-element vector between the i th and $(i+1)$ th nodes, and $\mathbf{x}_n^{(i)}(t)$ stands for the position vector of the i th node. More precisely, $L(t)$ tends to be an

² This is proportional to the integral scale of the two-point velocity correlation function in homogeneous isotropic turbulence.

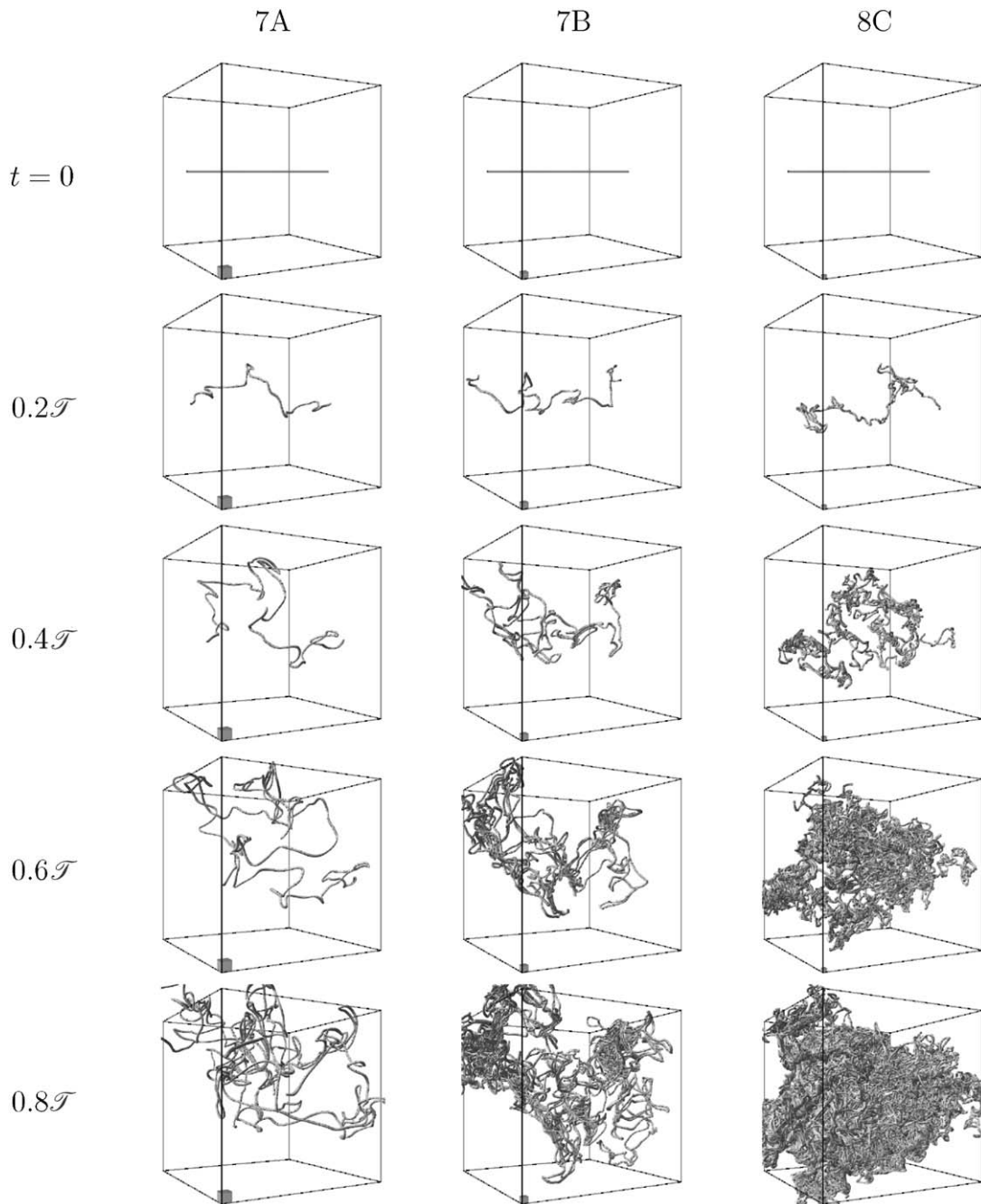


Fig. 1. Temporal evolutions of material lines. Large boxes represent the whole computational domain, while the side length of small boxes indicates 10η . Time elapses from top to bottom by $0.2\mathcal{T}$. Left column, run 7A; middle, run 7B; right, run 8C.

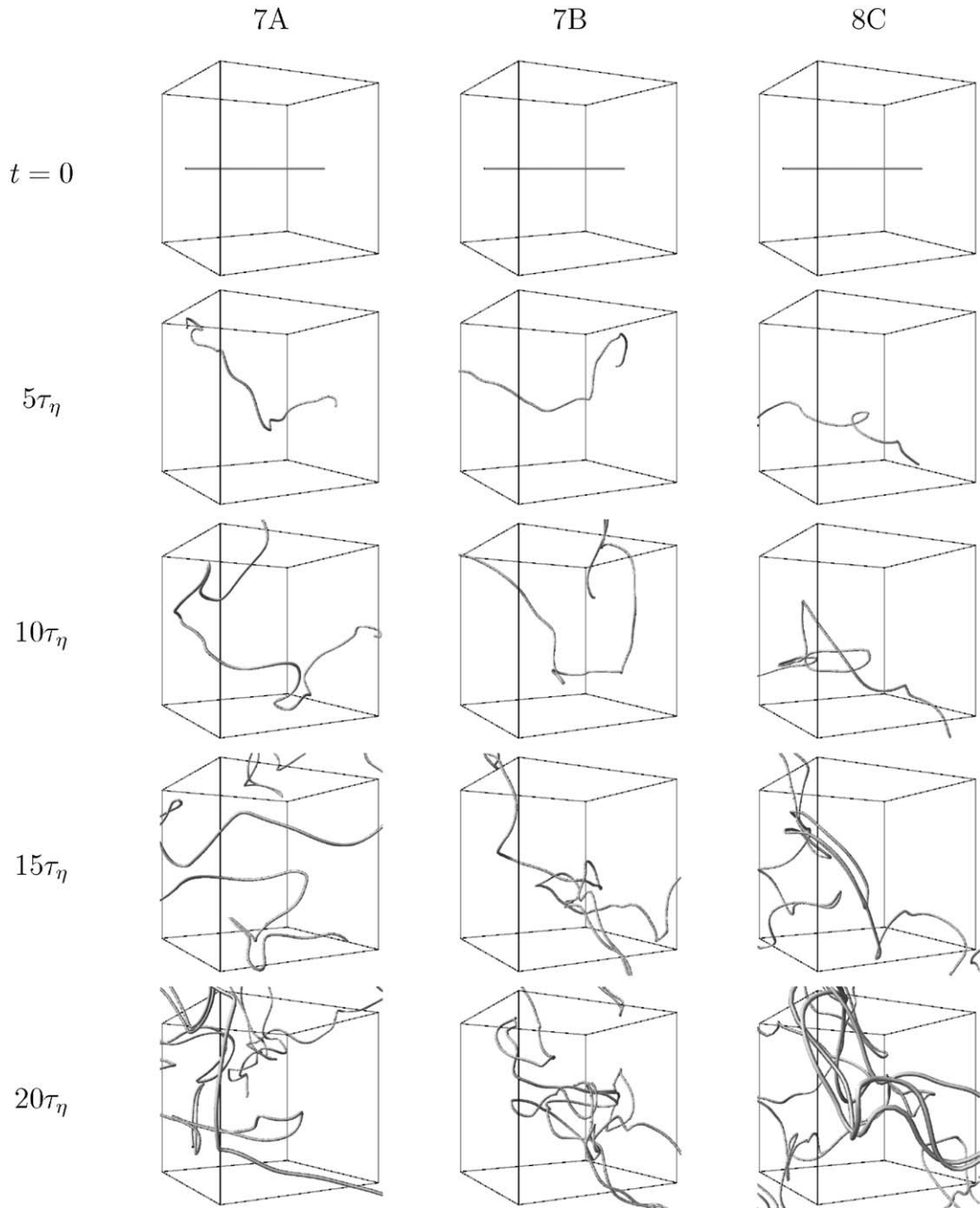


Fig. 2. Temporal evolutions of material lines viewed in the Kolmogorov-scale unit. The side length of boxes is 100η . Time elapses from top to bottom by $5\tau_\eta$. Left column, run 7A; middle, run 7B; right, run 8C.

exponential function for sufficiently large times, and the exponent (i.e., the stretching rate),

$$\gamma(t) = \frac{d}{dt} \log L(t), \quad (9)$$

has a larger value for a larger R_λ . See Fig. 4(a), below.

Note that statistics of the energy-containing-scale motions are almost independent of R_λ in the present DNS. That is, the eddy-turnover time \mathcal{T} and the energy-containing-scale length \mathcal{L} have very weak R_λ dependence, since both \mathcal{E} and ε hardly depend on R_λ as seen in Table 2. On the other hand, the Kolmogorov time τ_η and length η become smaller for larger R_λ . This is because the ratios \mathcal{T}/τ_η and \mathcal{L}/η are respectively proportional to R_λ and $R_\lambda^{3/2}$. Hence, the speed and complexity of material line deformations at larger R_λ imply that the deformation is governed by the small-scale fluid motions.

Next, let us turn our eyes to Fig. 2, in which temporal evolutions of material lines shown in Fig. 1 are viewed in Kolmogorov time and length units. The side length of the boxes shown in Fig. 2 is 100η of each flow, and the time increment between two vertically successive panels is $5\tau_\eta$. There seems to be no qualitative difference between these three temporal evolutions for different Reynolds numbers. In other words, the deformation of material lines in Kolmogorov units may be universal and independent of the Reynolds number. This is qualitatively consistent with Kolmogorov's similarity law for the statistics of material lines, which will be confirmed quantitatively in the following subsections.

In passing, we mention the behaviour of material lines on large scales. As seen in Fig. 1, spreading of the whole line is not so intensive, and seems to be independent of R_λ . Indeed, it is shown (figures are omitted) that temporal evolution of the gyration radius,

$$r(t) = \sqrt{\langle |\mathbf{x}_n(t) - \mathbf{x}_G(t)|^2 \rangle_{\text{line}}} \quad (10)$$

of the material line, $\mathbf{x}_G(t) = \langle \mathbf{x}_n(t) \rangle_{\text{line}}$ being the centre of gravity of the line, is independent of the Reynolds number, and tends to $r(t) \propto t^{1/2}$ at large t . This is reasonable because large-scale separation is described well as a random walk in contrast with the small-scale separation. Incidentally, the separation on the inertial scale should obey Richardson's law, i.e., proportional to $t^{3/2}$, and deformed material lines in such a scale range may have fractal structures. Measurement of the fractal dimension of deformed material objects is an interesting topic, and it is expected to be achieved in the near future by DNS which realizes a few decades of the inertial subrange.

3.2. Stretching rate

A typical time scale of deformation of a material line may be estimated by the reciprocal of the stretching rate γ defined by (9). The value of γ is calculated accurately by the following numerical analysis of the DNS data of many finite-length material lines. In the present DNS, each material line consists of N line elements³ and the stretching rate of each line element $\ell^{(i)}(t)$ can be

³ In order to keep the number of samples constant, we discard an endpoint of each material line, whenever a new node is added to interpolate a stretched part of the line. This implies that the present DNS simulates M material lines which are chopped, at every numerical time step, to have an approximately constant length of $O(\mathcal{L})$ because each line consists always of N nodes and the distance between two successive nodes is around the threshold (1.5 times the numerical grid width) of interpolation. Hence, we must notice that we deal with the statistics of such material lines that are artificially chopped. This point shall be taken up again in the last section.

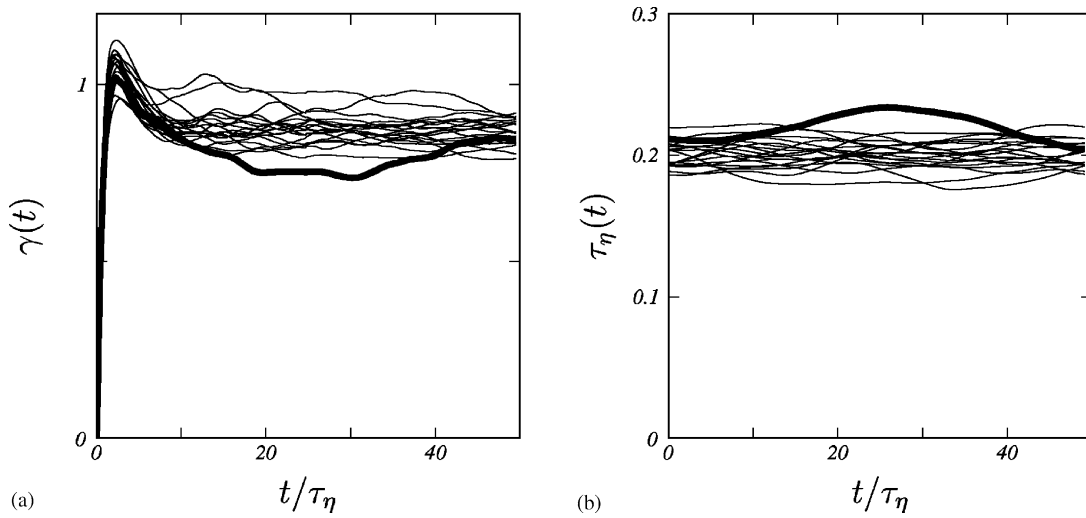


Fig. 3. (a) Temporal evolutions of stretching rate of material lines, which are obtained by the line average using 2×10^6 nodes, for 20 realizations. (b) The corresponding evolution of the Kolmogorov time. Thick curves indicate a same realization. Run 7A.

estimated by

$$\gamma_e^{(i)}(t) = \frac{d}{dt} \log \ell^{(i)}(t) = \frac{(\mathbf{u}(\mathbf{x}_n^{(i+1)}(t), t) - \mathbf{u}(\mathbf{x}_n^{(i)}(t), t)) \cdot (\mathbf{x}_n^{(i+1)}(t) - \mathbf{x}_n^{(i)}(t))}{|\mathbf{x}_n^{(i+1)}(t) - \mathbf{x}_n^{(i)}(t)|^2} \quad (11)$$

in terms of the position vectors $\mathbf{x}_n^{(i)}(t)$ and the advection velocities $\mathbf{u}(\mathbf{x}_n^{(i)}(t), t)$ of the line nodes. We track simultaneously M ($= 2^{14}$ for runs 7A, 7B, 8C, and $= 2^{12}$ for 9D, 9E) lines in each simulation (see Table 1). Using the relation

$$\gamma(t) = \langle \gamma_e(t) \rangle_{\text{line}} \left(= \frac{\sum_{i=1}^{NM} \gamma_e^{(i)}(t) \ell^{(i)}(t)}{\sum_{i=1}^{NM} \ell^{(i)}(t)} \right), \quad (12)$$

which is derived from (8), (9) and (11), we can accurately evaluate γ as the line average of γ_e . Although the total number NM , which is $O(10^6)$ for all cases,⁴ seems to be large enough to estimate the line average, the fluctuation of $\gamma(t)$ is substantial, as seen in Fig. 3(a). This large temporal fluctuation of $\gamma(t)$ synchronizes with that of the Kolmogorov time (Fig. 3(b)). When $\tau_\eta(t)$ is larger, then $\gamma(t)$ is smaller, and vice versa (cf. the thick curves in Figs. 3(a) and (b)). This is consistent with Kolmogorov’s similarity law. Hence, we further take an ensemble average of $\gamma(t)$ over 20 realizations for each Reynolds number. The results are plotted in Fig. 4(a). As expected from the discussion in the preceding subsection, the stretching rate is larger at higher Reynolds numbers, that is, the time scale of deformation of material lines is smaller. According to Kolmogorov’s similarity law, when the time and the stretching rate are respectively normalized by τ_η and τ_η^{-1} , the temporal

⁴ $NM = 2,097,152$ for $N = 128$ (runs 7A, 7B), $4,194,304$ for $N = 256$ (run 8C), and $2,097,152$ for $N = 512$ (runs 9E, 9D).

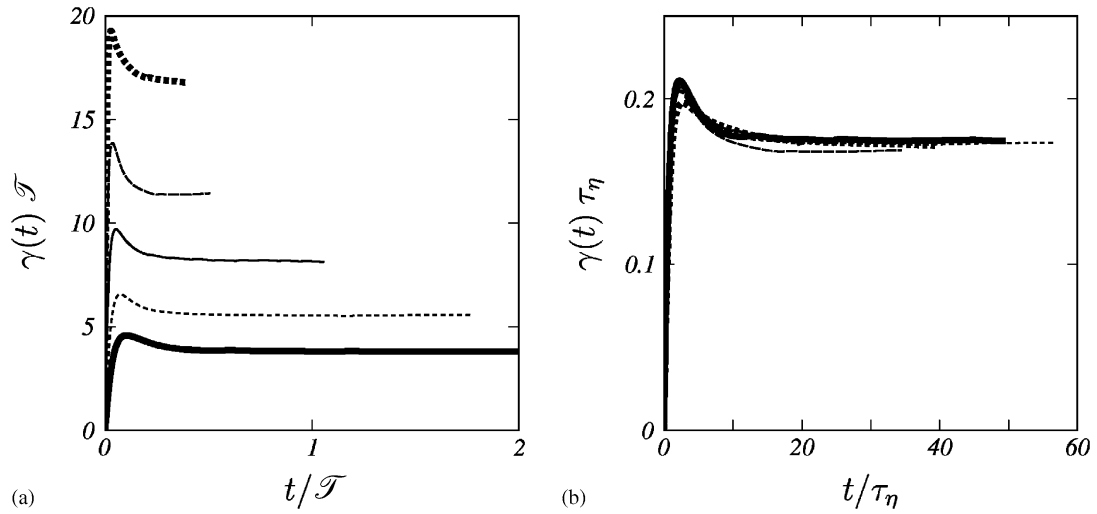


Fig. 4. Ensemble average of temporal evolution of stretching rate of material lines. The time and the stretching rate are normalized by (a) the energy-containing-scale time and its reciprocal, and (b) the Kolmogorov time and its reciprocal. Thick curve, run 7A; thin dotted, run 7B; thin, run 8C; thin dashed, run 9D; thick dotted, run 9E.

Table 3

Statistics of material lines. The temporal average in the statistically stationary period ($t \gtrsim 20\tau_\eta$) of the mean and the standard deviation of stretching rate γ and curvature α of material lines over $J = 20$ realizations

Runs	$\gamma\tau_\eta$	$\alpha\eta$	$\alpha\lambda$
7A	0.174 ± 0.009	0.0976 ± 0.0030	1.44 ± 0.04
7B	0.174 ± 0.007	0.0955 ± 0.0025	1.71 ± 0.05
8C	0.175 ± 0.012	0.0931 ± 0.0043	2.02 ± 0.09
9D	0.169 ± 0.014	0.0907 ± 0.0027	2.36 ± 0.07
9E	0.173 ± 0.010	0.0994 ± 0.0045	3.10 ± 0.14

evolutions of stretching rate should be independent of the Reynolds number. This is the case as shown in Fig. 4(b). The stretching rate starts from zero, peaks around $t \approx 5\tau_\eta$, and settles down to a stationary value after $t \gtrsim 20\tau_\eta$. A constant value of stretching rate implies that the total length of material lines increases exponentially in time.

Temporal averages of $\gamma(t)$ normalized by τ_η^{-1} in the statistically stationary state ($t \gtrsim 20\tau_\eta$) are listed in Table 3. Since there is no systematic dependence of the average values on the Reynolds number, we may conclude that the time scale of deformation of material lines is around $(1/0.17 = 5.9)\tau_\eta$, which is also comparable to the time scale to forget the initial conditions, i.e., the time scale to settle down to the statistically stationary state (Fig. 4(b)) and also the auto-correlation time of stretching rate of material elements (Fig. 5 of Goto and Kida, 2002).

The probability density functions (PDF) of the local stretching rate γ_e normalized by τ_η^{-1} are plotted in Fig. 5(a) for the five cases. They are also independent of R_λ , implying to obey Kolmogorov's similarity law. However, careful observation of the PDF on a semi-logarithmic scale reveals that the fluctuation becomes larger for larger Reynolds number cases (Fig. 5(b)). In this sense, the

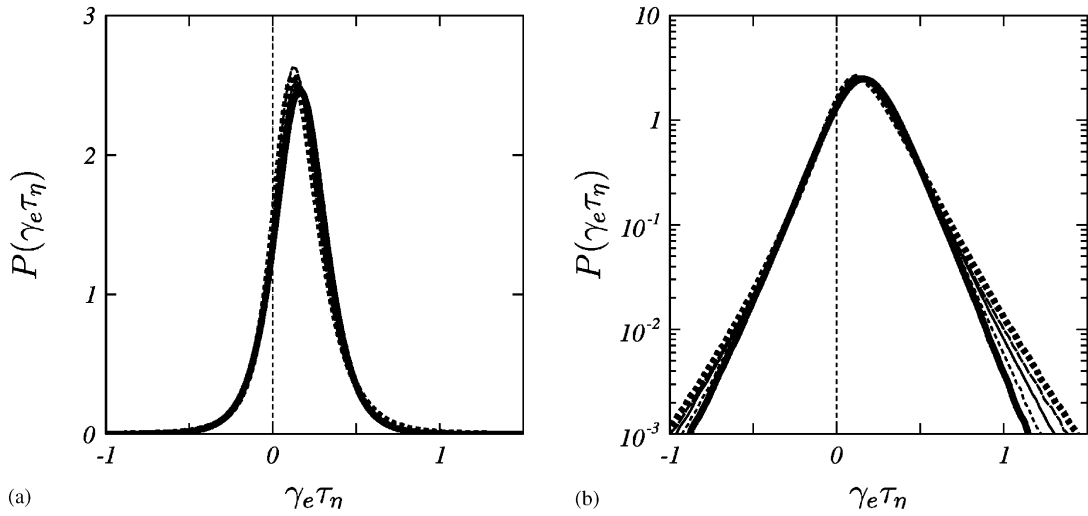


Fig. 5. PDF of local stretching rate of material lines for five different Reynolds numbers. Each curve is obtained by taking an average over 20 realizations. Thick curve, run 7A; thin dotted, run 7B; thin, run 8C; thin dashed, run 9D; thick dotted, run 9E.

Kolmogorov similarity of stretching rate of material lines suffers a correction by the intermittency effect similar to the well-known fact that the flatness of velocity gradient increases with the Reynolds number.

3.3. Curvature

Material lines are stretched locally by Kolmogorov-scale eddies, and it is expected that the characteristic length of the lines is proportional to the Kolmogorov length. In order to estimate the (reciprocal of) length scale, we calculate the local curvature,

$$\alpha_e(s, t) = \sqrt{\left| \frac{\partial^2}{\partial s^2} \mathbf{x}_n(s, t) \right|^2}, \tag{13}$$

where s is a coordinate taken along a material line. In the present DNS, this local curvature $\alpha_e^{(i)}(t)$, at the i th material line element, is estimated by the position vectors of three successive nodes along the line. Then their line average,

$$\alpha(t) = \langle \alpha_e(t) \rangle_{\text{line}}, \tag{14}$$

gives the mean curvature of material lines. Similarly to the stretching rate, in spite of largeness of the number of line segments, $NM = O(10^6)$, the value of $\alpha(t)$ exhibits relatively large fluctuations, which may be caused by large fluctuations of $\eta(t)$. Hence, we take an average of $\alpha(t)$ over 20 realizations with different initial velocity fields for each Reynolds number. The result is plotted in Fig. 6(a). Initially, the material lines are straight, and therefore their curvatures vanish. As time progresses, the curvatures increase rapidly and saturate to constant values which are larger for larger R_λ as expected from Fig. 1.

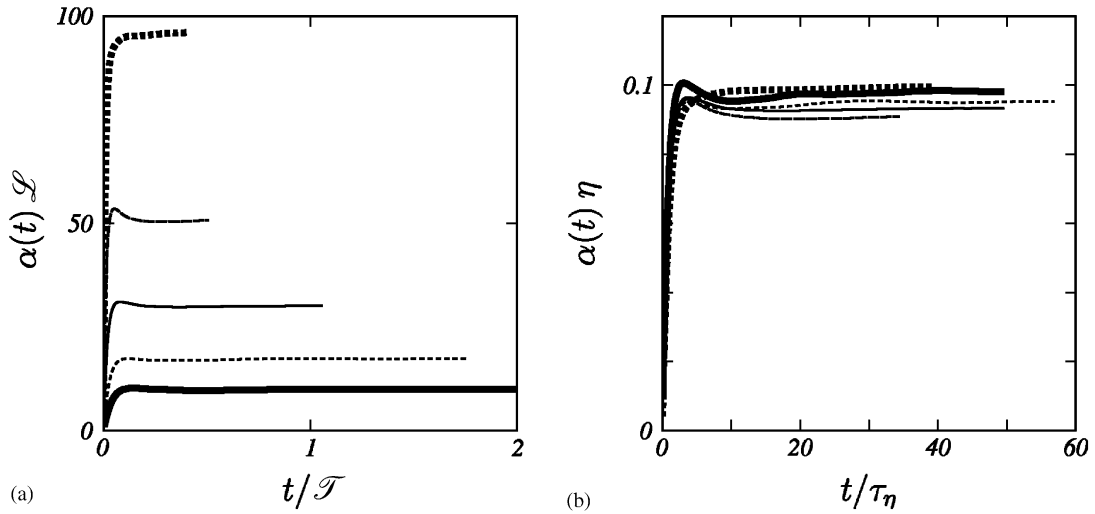


Fig. 6. Ensemble average of temporal evolution of mean curvature of material lines. The time and the curvature are normalized by (a) the energy-containing-scale time and the reciprocal of the energy-containing-scale length, and (b) the Kolmogorov time and the reciprocal of the Kolmogorov length. Thick curve, run 7A; thin dotted, run 7B; thin, run 8C; thin dashed, run 9D; thick dotted, run 9E.

According to Kolmogorov's similarity law, the five curves in Fig. 6(a) should coincide with each other when the abscissa and the ordinate are normalized by τ_η and η^{-1} , respectively. This is the case as shown in Fig. 6(b). The normalized value $\alpha(t)\eta$ takes a peak around $t \approx 5\tau_\eta$ and settles down around $0.1\eta^{-1}$ after $t \gtrsim 20\tau_\eta$. The temporal averages of $\alpha(t)$ normalized by η^{-1} in the statistically stationary state ($t \gtrsim 20\tau_\eta$) are listed in Table 3. There seems to be no systematic Reynolds number dependence, and therefore we may conclude that the characteristic length of deformation of material lines is around 10η . The Kolmogorov similarity is also observed in the PDF of local curvature normalized by η^{-1} of material lines. We plot it in Fig. 7 for five different Reynolds numbers. All the curves are in good agreement with each other, although small deviations of the curve for the largest Reynolds number may be observed in the semi-logarithmic plots. In contrast with the local stretching rate (Fig. 5), fluctuations of the local curvature seem not to become larger with increasing Reynolds number. Note that the universality of the curvature of material lines is less excellent than that of the stretching rate seen in the preceding subsection (cf. Figs. 4(b) and 6(b)). This may be attributed to the large fluctuations of α_e compared with γ_e (cf. the slopes of the tails of PDFs in Figs. 5(b) and 7(b)). Incidentally, the temporal average of the mean curvature $\alpha(t)$ normalized by the reciprocal of the temporal average of the Taylor length λ increases monotonically with the Reynolds number (see the last column in Table 3). This implies that the curvature does not scale with λ . These results lead us to the conclusion that the material line deformations are characterized by the Kolmogorov scales.

Finally, we point out a remarkable feature observed in the joint statistics of stretching rate and the curvature of material lines. The joint PDF $P(\alpha_e, \gamma_e)$ is plotted in Fig. 8 together with the conditional average $\langle \gamma_e | \alpha_e \rangle_{\text{line}}$ of the stretching rate for a given curvature for five different Reynolds numbers. The PDF is independent of the Reynolds number, and the stretching rate and the curvature are

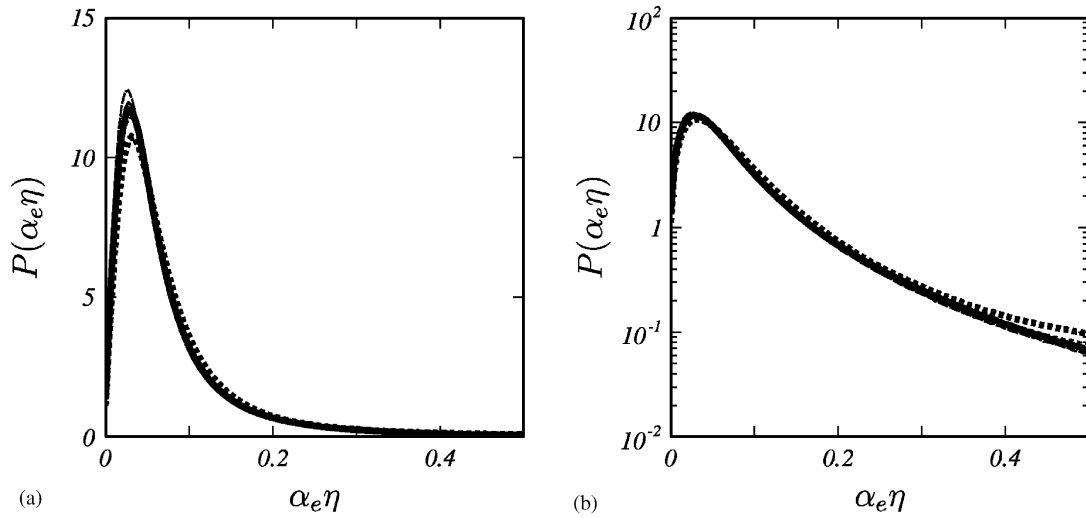


Fig. 7. PDF of local curvature of material lines for five different Reynolds numbers. Each curve is obtained by taking an average over 20 realizations. Thick curve, run 7A; thin dotted, run 7B; thin, run 8C; thin dashed, run 9D; thick dotted, run 9E.

negatively correlated, namely, the stretching rate takes larger values in the relatively straight regions of material lines. We will return to this point in Section 5.2 when we discuss the physical mechanism of material lines from the viewpoint of the dynamical role of small-scale coherent vortices. The evolution equation for the local curvature of material lines (see Drummond and Münch, 1991) describes the suppression of local curvature by positive local stretching.

3.4. Alignment

Since the stretching rate of material lines is one of the most important statistical quantities of the present system, many attempts have been made to predict its value theoretically. A conventional strategy is the one based upon the alignment between the tangential vector of the material line and eigenvectors of the rate-of-strain tensor \mathbf{S} , since the stretching rate $\gamma_e(t)$ of a line element can be expressed in terms of \mathbf{S} as

$$\begin{aligned} \gamma_e &= \frac{\mathbf{l} \cdot \mathbf{S} \cdot \mathbf{l}}{\ell^2} = s_1 \cos \theta_1 + s_2 \cos \theta_2 + s_3 \cos \theta_3 \\ &= s_1 \sin \theta_3 \cos \varphi + s_2 \sin \theta_3 \sin \varphi + s_3 \cos \theta_3, \end{aligned} \tag{15}$$

where s_1, s_2, s_3 ($s_1 \geq s_2 \geq s_3$) are eigenvalues of \mathbf{S} , and $\theta_1, \theta_2, \theta_3$ are angles between $\mathbf{l}^{(i)}(t)$ and the respective eigenvectors of \mathbf{S} . The spatiotemporal averages of the eigenvalues are $\langle s_1 \rangle = 0.4\tau_\eta^{-1}$, $\langle s_2 \rangle = 0.1\tau_\eta^{-1}$ and $\langle s_3 \rangle = -0.5\tau_\eta^{-1}$, which are approximately independent of the Reynolds number in the range considered. The angle φ is defined in Fig. 9(f). Thanks to expression (15), if material line elements tended to align to the eigenvectors in a simple manner, as assumed in classical theories (e.g., Batchelor and Townsend, 1956), a theoretical prediction of the stretching rate would be possible. However, as seen in Fig. 9, the alignment between the tangent vectors and the eigenvectors seems

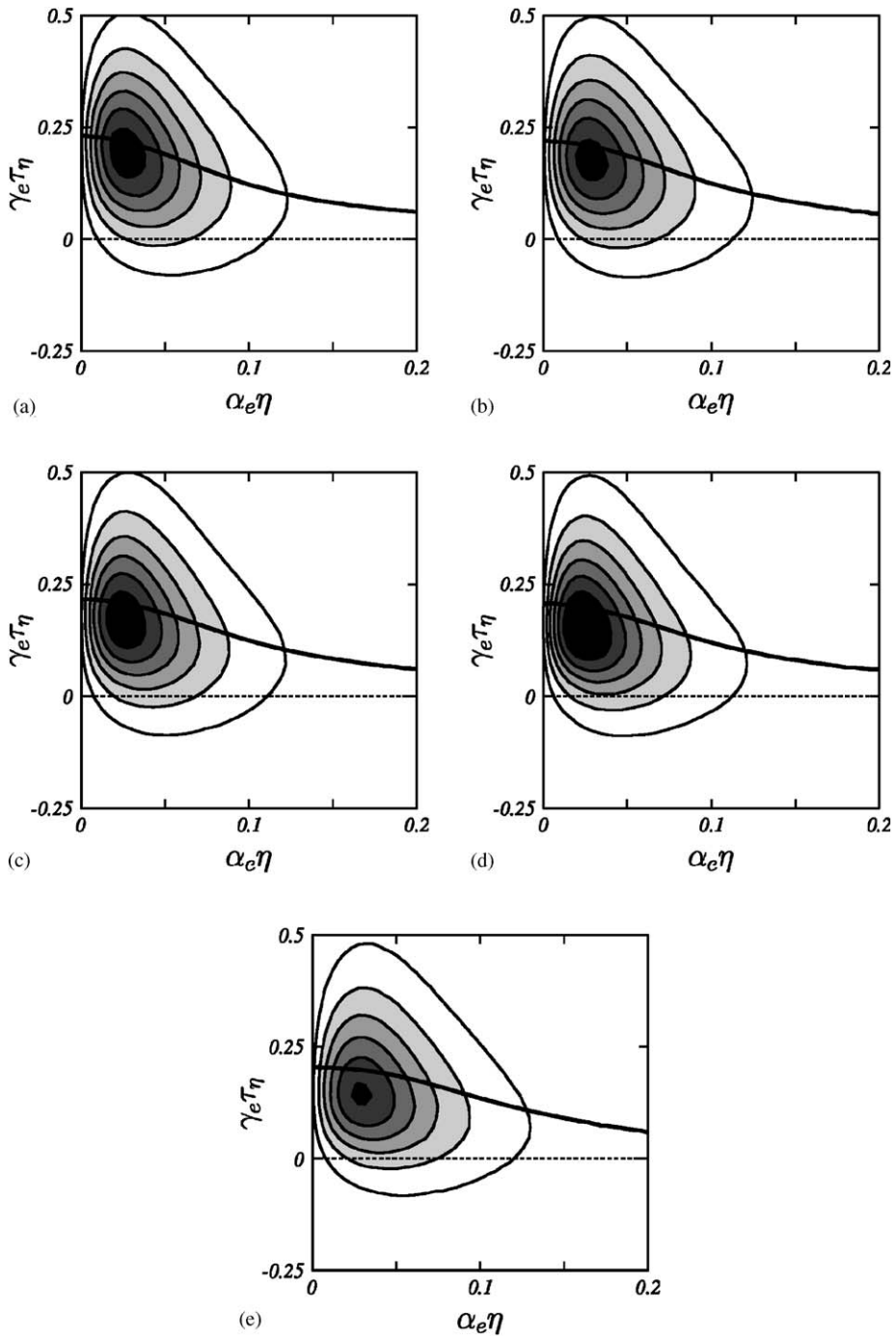


Fig. 8. Joint PDF of local curvature α_e and local stretching rate γ_e of material lines. (a) Run 7A, (b) run 7B, (c) run 8C, (d) run 9D, (e) run 9E. Contour levels are $5n$ ($n = 1, \dots, 6$). The thick curve denotes the conditional average of γ_e for fixed α_e . Averages are over 20 realizations.

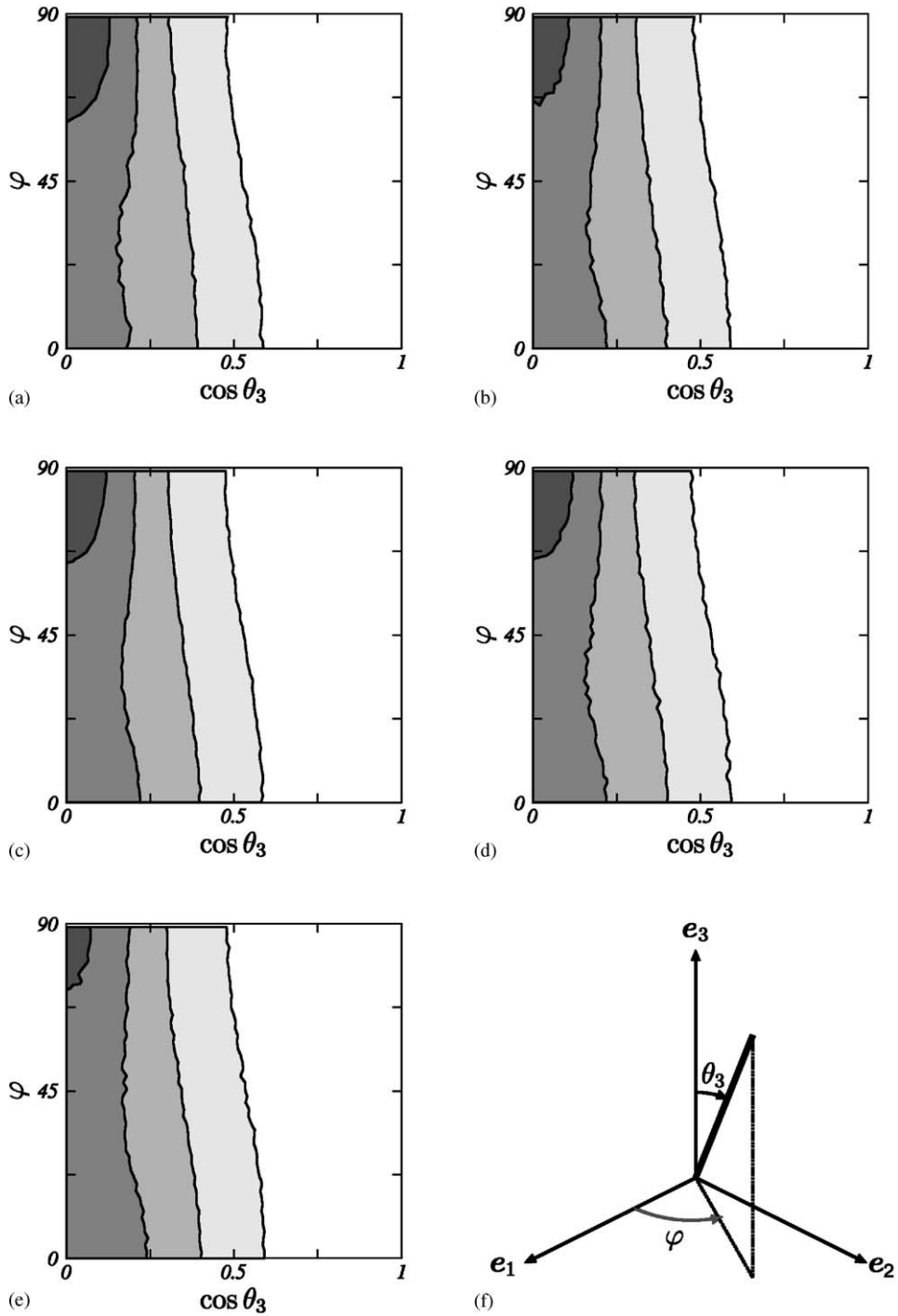


Fig. 9. PDF of the angles between the eigenvectors of the rate-of-strain tensor and the tangent vector of a material line. Average over 10 snapshots. Contour levels are $0.4n$ ($n = 1, 2, 3, 4$). (a) Run 7A, (b) run 7B, (c) run 8C, (d) run 9D, (e) run 9E, (f) definitions of θ_3 and φ , where e_1 , e_2 and e_3 are the three eigenvectors of the rate-of-strain tensor.

too complicated to construct a theory. Nevertheless, we emphasize that the alignment is quite robust. In other words, the PDF of each snapshot at any time at any Reynolds number is almost identical in the statistically stationary state. This is because the alignment property is related to neither the magnitude of η nor that of τ_η in contrast with the stretching rate and the curvature.

4. Antiparallel pairs of tubular vortices

It was shown in the preceding section that material line stretching is strongly related to small-scale fluid motions. Recall that there exist coherent vortical structures in small scales of turbulence. Hence, it is expected that we may understand the physical mechanism of material line deformations as a dynamical role of the small-scale coherent structures. Before going into detailed discussions on the dynamical roles, we describe the statistics of coherent structures in this section. We will pay special attention to clusters of the coherent vortical structures.

4.1. Small-scale tubular vortices

Since the discovery of small-scale coherent vortical structures in homogeneous isotropic turbulence in the 1980s, many kinds of identification methods of the structures have been proposed by many authors (see Kida and Miura, 1998a, and references therein), and their statistics have been intensively investigated. In the present study we adopt the low-pressure criterion (Miura and Kida, 1997) because it is highly objective and free from a threshold of any quantity. Details of its identification algorithm are given in Kida and Miura (1998b), but we recapitulate it here for completeness of the present article. The algorithm consists of the following two steps. In the first step, we extract the axes of the tubular vortices by searching a chain of local pressure minimum points. Here, the local minimum means that the pressure takes a minimum locally on a plane associated with two eigenvectors of the pressure hessian. An axis is constructed by connecting the pressure minimum points in the direction of the third eigenvector of the hessian. A line connecting two successive points is called the segment, the length of which is of order of the numerical grid width. In the second step, we demarcate the core of each vortex by applying the pressure convexity condition around each axis constructed in the first step. In Fig. 10, we draw typical vortical structures identified by the low-pressure criterion for two different Reynolds numbers, $R_\lambda = 84$ and 175. The well-known tubular structures at small scales, called the worms, are clearly captured. In Figs. 10(a) and (c), the side lengths of larger boxes are $\mathcal{L}/2$ and $\mathcal{L}/3$, respectively, while those of smaller boxes are 10η of each flow. Note that radii of the tubular vortices are comparable to the Kolmogorov length, while some vortex tubes extend as long as the integral length. In this sense, these tubular vortical structures are small in cross-section, but not small in general in the longitudinal direction.

Statistics of individual tubular vortices have been recently investigated, by comparing three cases of different Reynolds numbers between $R_\lambda = 84$ and 175, leading to the conclusion that the mean radius is $a \approx 5\eta$ and the mean circulation is $\Gamma \approx 110\nu$ irrespective of the Reynolds number (Makihara and Kida, 2003). These results imply that the cross-sectional structure of the tubular vortices is characterized by the Kolmogorov variables. For example, the mean swirling velocity at the core boundary of vortices is $\Gamma/2\pi a \approx 3.5\eta/\tau_\eta$. Although this conclusion should be taken with reservation because of the limited range of Reynolds number examined, it is certain that in contrast to the

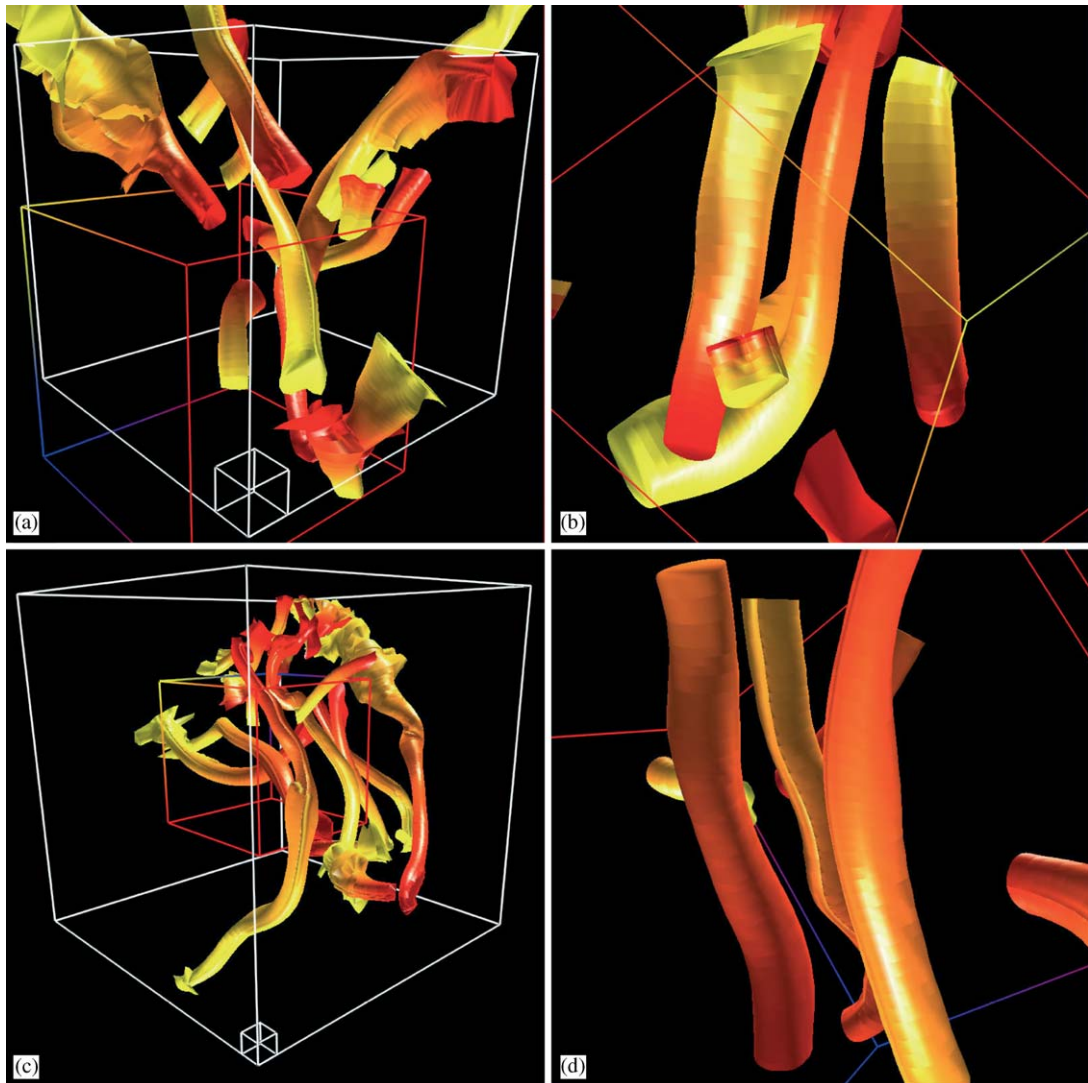


Fig. 10. Clusters of tubular vortices identified by the low-pressure criterion. Only the vortices within 25η from the central vortex are drawn in (a) and (c). The vorticity vector points approximately along the tube from red to yellow. (a), (b) $R_\lambda = 84$; (c), (d) 175. In (a) and (c), side lengths of larger white boxes are $\mathcal{L}/2$ and $\mathcal{L}/3$, respectively, while those of smaller white boxes are 10η of each flow. Figures (b) and (d) are respectively parts of (a) and (c) cropped by the coloured cube shown with side of 75η . Different colours are used for the edges of the cubes so that their relative orientations between (a) and (b) and between (c) and (d) can easily be recognized.

cross-sectional structure of the vortices, their longitudinal length does not obey the Kolmogorov statistics. It may be observed in Figs. 10(a) and (c) that the lengths of the tubular vortices vary between $O(\eta)$ and $O(\mathcal{L})$. Recall that the statistics of material line stretching obey Kolmogorov's similarity law. These observations, therefore, suggest that material line deformations are closely related to the flow structure perpendicular to the tubular vortices.

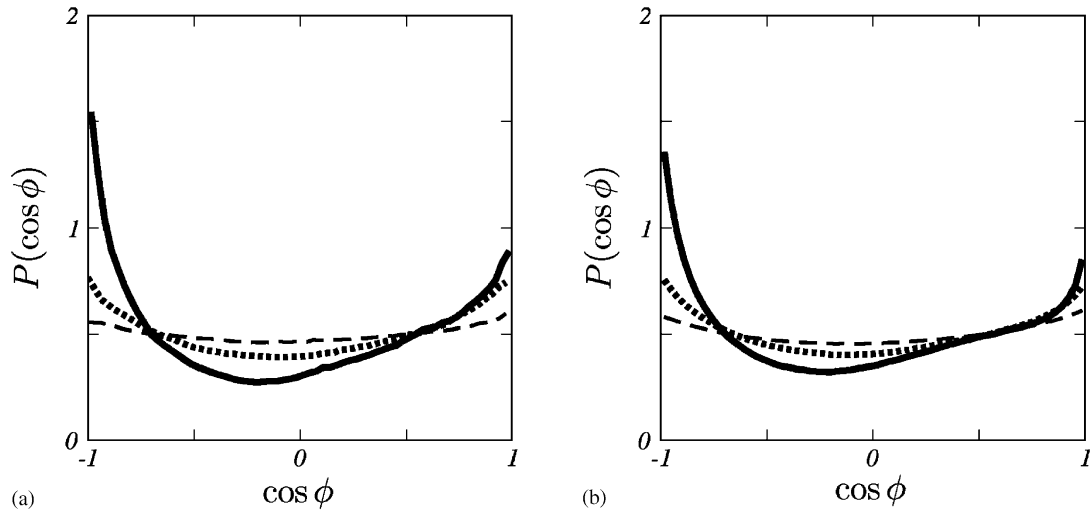


Fig. 11. PDF of the cosine of angle ϕ between pairs of tubular vortices conditioned by distance d between them. Solid curve, $d/\eta \leq 20$; dotted, $20 \leq d/\eta \leq 40$; dashed, $40 \leq d/\eta \leq 60$. (a) $R_\lambda = 84$. Averaged over 200 snapshots. (b) $R_\lambda = 175$. Averaged over 17 snapshots.

4.2. Antiparallel pairs

In Figs. 10(a) and (c), we draw tubular vortices which are located within 25η from the central relatively longer vortex. Each vortex core is coloured to indicate the direction of swirling around it. That is, the vorticity vector approximately points from red to yellow. Careful observation of these figures reveals that the surrounding vortices align antiparallel to the central one. Figs. 10(b) and (d) are parts of (a) and (c), respectively, where each cluster is cropped by a coloured cube with side of 75η . Antiparallel alignments are clearly seen of the vortices on both sides of the central one in Fig. 10(b) and of the left two vortices to the right one in Fig. 10(d). This antiparallel alignment will be shown, in the next section, to play crucial roles in the strong stretching of material lines. It is also interesting to observe that there is no difference in appearances of the vortical structures on the Kolmogorov scales between Figs. 10(b) and (d). This is similar to the case of material line deformations as seen in Fig. 2, and offers evidence that material line deformations are governed by these vortical structures.

The tendency of antiparallel alignment of tubular vortices is quantitatively confirmed by evaluating the PDF of the cosine of angle ϕ between pairs of vortices. The PDF, plotted in Fig. 11 for two Reynolds numbers, is conditioned by the distance d between them. Here, ϕ and d are respectively defined by the angle and the distance between axis segments of a pair of tubular vortices, the centre of one of which is located between two parallel planes crossing perpendicularly the two endpoints of the other. In evaluation of the PDF, we have ignored vortices shorter than 10η of each flow because such vortices do not have tubular shapes, and the sign of the cosine is determined by the directions of the vorticity vectors at the two segments, i.e., $\cos \phi = -1$ (or 1) indicates the antiparallel (or the parallel) alignment. The PDF for the near region $d \leq 20\eta$ has the highest peak at $\cos \phi = -1$ and the second highest at $\cos \phi = 1$, implying that the antiparallel alignment is most probable and the

parallel alignment is also highly probable. By comparing the three curves, we find that as the distance between two segments increases, the PDF approaches a flat distribution with the direction of vortices distributed isotropically. The PDFs shown in Figs. 11(a) and (b) are conspicuously similar, where the Reynolds number for the latter is twice that for the former. The tendency of the antiparallel alignment of nearby vortices, therefore, is likely independent of the Reynolds number.

The tendency of antiparallel alignments of tubular vortices has been shown both qualitatively in Fig. 10 and quantitatively in Fig. 11. Some examples of an antiparallel approach of vortices are captured by automatic tracking of identified tubular vortices (Kida et al., 2001; Makihara et al., 2002). The antiparallel approach may be understood by the same explanation as in the case of infinitesimally thin vortex filaments in an ideal fluid (Siggia, 1985). However, in contrast to vortex filaments in an ideal fluid, tubular vortices in a viscous fluid can be generated or destroyed by the flow field induced by themselves. Therefore, some mechanisms of the approach other than the above one may exist to explain the antiparallel alignment of nearby vortices. Understanding of the detailed physical mechanism of the antiparallel alignments is left for future studies. It is, however, worth noting that through a number of visualizations, we obtain an impression that three or four, rather than two, vortices frequently gather in antiparallel, and necessarily parallel, manners. This tendency is clearly observed also in the examples given in Fig. 10, and may offer a reason for the other peak at $\cos \phi = 1$ in Fig. 11 corresponding to the parallel alignments.

4.3. Cross-sectional flow structure

As was mentioned in Section 4.1, the stretching of material lines is likely related to the cross-sectional flow structure of tubular vortices, since statistics of both quantities are characterized by the Kolmogorov variables. On the other hand, the tendency of the alignment of tubular vortices in parallel or antiparallel manner, observed in the preceding subsection, implies that a cross-section is sometimes sheared by a few approximately aligned tubular vortices. These two facts encourage us to investigate cross-sectional flow structures around a tubular vortex. In Fig. 12, we show the flow field on a cross-section of an arbitrarily chosen tubular vortex which is located at the centre, where the vorticity component normal to the cross-section, magnitude of the vorticity component parallel to the cross-section, the relative velocity to the centre and the magnitude of strain rate are plotted in (a)–(d), respectively.

The side length of the cross-sections shown in Fig. 12 is about 50η , which is appropriate to capture the cross-sectional structure of a vortex cluster. Recall that the alignment of vortices is conspicuous in the near region $d \lesssim 20\eta$ (Fig. 11). As expected from the argument in the preceding subsection, it is not difficult to find antiparallel vortex pairs on an arbitrary cross-section of any vortex as in this figure. The normal component, shown in Fig. 12(a), of vorticity has the highest positive peak around the centre at which the chosen vortex is located, and two low negative peaks in the upper-right and the lower-left quadrants where antiparallel vortices are located. The relative velocity field shown in Fig. 12(c) may be regarded as the one induced by these three vortices, where two elliptic stagnation points (denoted by solid circles) around the centres of the central and upper-right vortices, and two hyperbolic stagnation points (denoted by solid squares) between them are observed. It should be noted here that an antiparallel vortex pair produces a strong strain field near the hyperbolic stagnation points, as shown in Fig. 12(d).

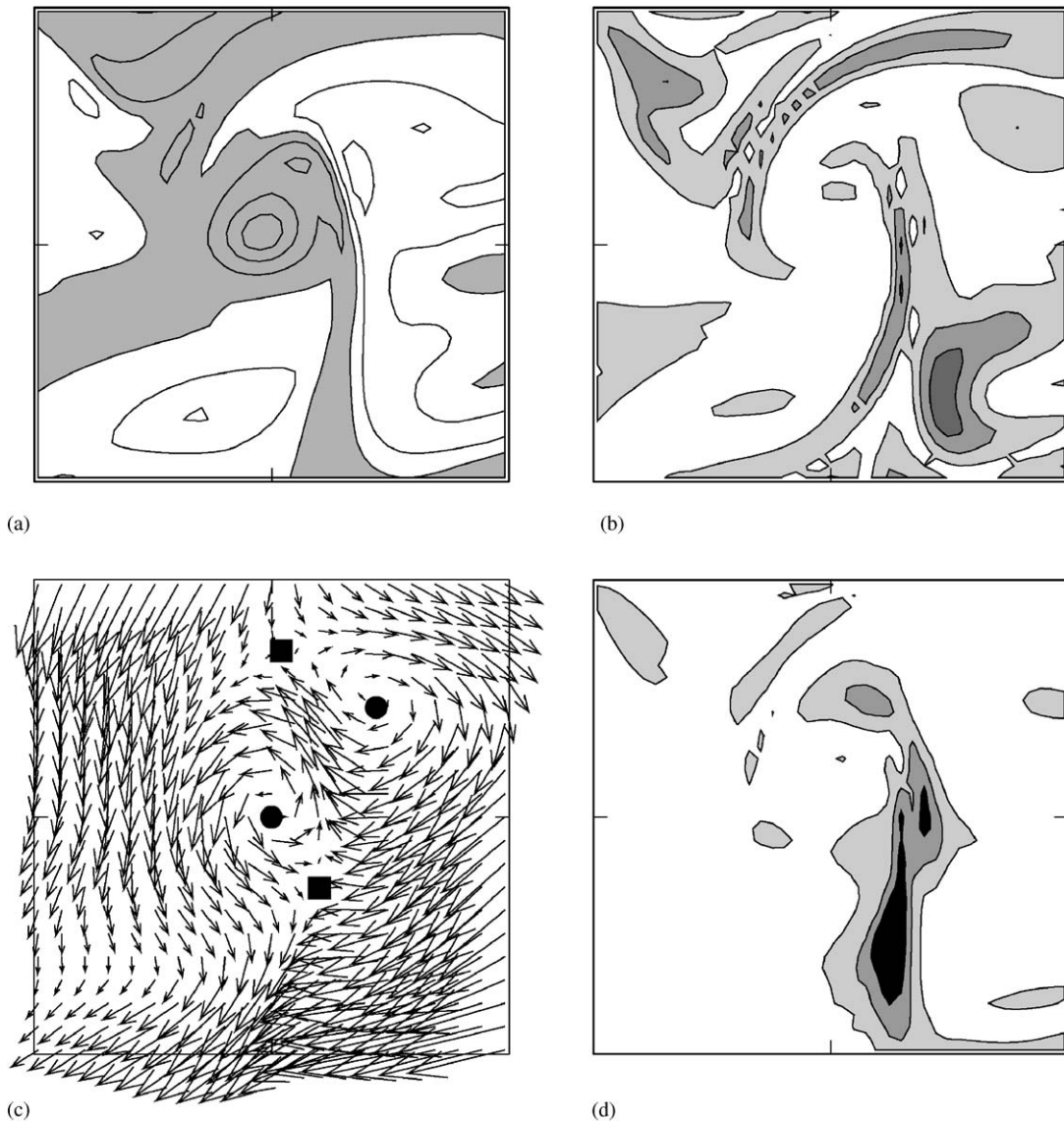


Fig. 12. Cross-sectional flow structure around a tubular vortex. (a) Vorticity component normal to the cross-section. Contour levels are $\pm n\tau_\eta^{-1}$ ($n = 0, 1, 2, 3$). Around the central vortex, there exist two vortices of opposite sign of vorticity in the upper-right and lower-left quadrants. (b) Magnitude of vorticity component parallel to the cross-section. Contour levels are $0.5n\tau_\eta^{-1}$ ($n = 1, 2, 3$). Double spirals are clearly observed. (c) Velocity field relative to that at the centre. Hyperbolic and elliptic stagnation points are denoted by solid squares and solid circles, respectively. (d) Magnitude of strain rate. Contour levels are $n\tau_\eta^{-2}$ ($n = 1, 2, 3$). In shaded regions the field quantity takes positive values in (a) and larger values in (b) and (d). The side length of the squares is about 50η . $R_\lambda = 84$.

In order to illustrate that a pair of antiparallel vortices is always accompanied by two strong strain regions between them, we draw, in Fig. 13, an ideal flow field induced by two antiparallel vortex tubes with a Gaussian vorticity distribution. Fig. 13(a) shows the vorticity field and the relative

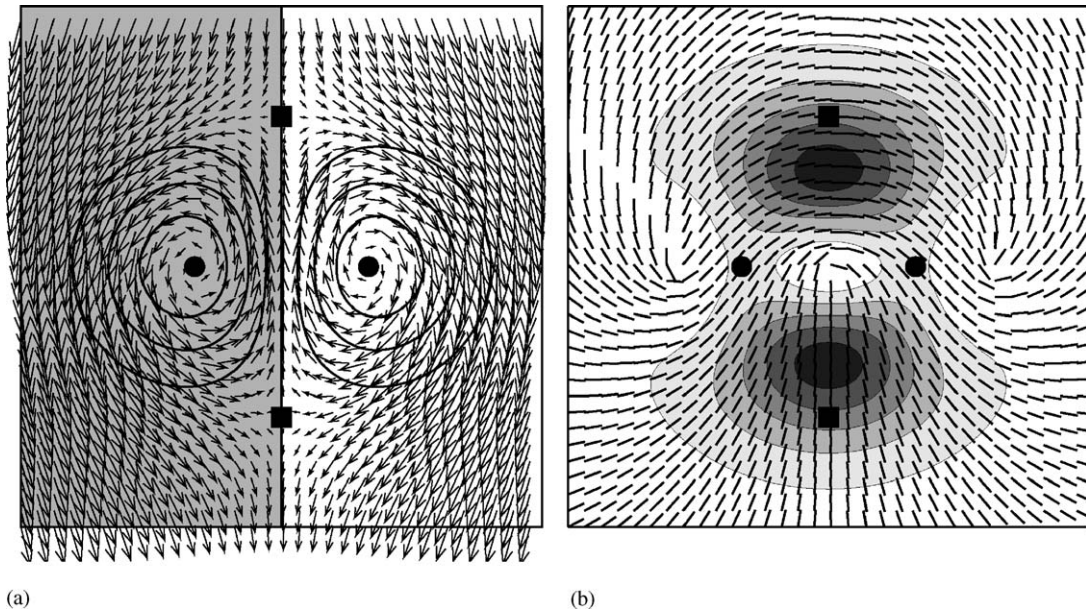


Fig. 13. An antiparallel pair of vortex tubes with a Gaussian vorticity distribution. (a) The relative velocity field (arrows) and the vorticity field (contours). There are elliptic (solid circles) and hyperbolic (solid squares) stagnation points observed in the coordinate system moving with the vortices. (b) The magnitude of strain (contours) and the directions of the eigenvectors (lines) associated with positive eigenvalues of the rate-of-strain tensor.

velocity to the centres of the vortices. As in the case of the real flow shown in Fig. 12(c), the elliptic (denoted by solid circles) and the hyperbolic (denoted by solid squares) stagnation points exist on the frame moving with the vortex centres. Fig. 13(b) clearly shows that the vortex pair produces two strong strain regions near the hyperbolic stagnation points. As was seen in (15), strong strain is necessary for intensive stretching of material lines. It must be emphasized, however, that the strong strain is necessary but not sufficient. Only when the material line aligns with the eigenvector associated with the largest positive eigenvalue of the rate-of-strain tensor, they are stretched intensively. Note that the directions of the eigenvectors, shown in Fig. 13(b), are approximately horizontal in the upper strong strain region, and approximately vertical in the lower one. Hence, we expect that if the material lines are stretched strongly in such regions, then the strong stretched parts of material lines take a T-shaped form. It will be seen in the next section (see Figs. 14 and 16(a)) that this is indeed the case. It is likely that the flow field around an antiparallel vortex pair not only induces two strong strain regions, but also makes material lines align to the eigenvectors in such regions. This is related to the fact that the streamlines are nearly parallel to the eigenvectors around the hyperbolic stagnation points. Note that a material line element parallel to a trajectory, which coincides with the streamlines in a stationary system, is always on the trajectory.

It will be shown in the next section that such strong strain regions near hyperbolic stagnation points produced by antiparallel vortex pairs play a crucial role in the stretching of material lines. The component of vorticity parallel to the cross-section also takes larger values in the strong strain regions. This is reasonable since the vorticity stretching on the cross-section is enhanced, similarly to

the stretching of material lines, in the strong strain regions in the direction of the eigenvectors. Indeed, it is observed in Fig. 12(b) that in a T-shaped region, which is however being deformed substantially due to the difference in strength of the central and the upper-right vortices, the cross-sectional component of vorticity takes large values. Such regions of strong cross-sectional vorticity component around a tubular vortex were reported as the double spiral structures in Kida and Miura (2000). The generation mechanism of such double spiral structures should be explained in terms of the strong strain region formed near the hyperbolic stagnation points between an antiparallel pair of tubular vortices. Needless to say, strong strain means strong energy dissipation. Hence, the strong strain regions between antiparallel vortex pairs play important roles in various aspects such as enhancement of stretching of material objects, generation of cross-sectional vorticity component, effective energy dissipation, and so on.

5. Stretching enhancement by antiparallel vortex pairs

A frequently used phrase “deformations of material lines are governed by small-scale eddies” now possesses a concrete meaning. The purpose of this section is to illustrate this picture clearly by detailed analyses of DNS data of material lines. It was shown in the preceding section that small-scale eddies have tubular shapes with radii of $O(5\eta)$ and lengths ranging from $O(\eta)$ to $O(\mathcal{L})$, and that they tend to align antiparallel to each other in the near region $d \lesssim 20\eta$. The cross-sectional flow field reveals a remarkable structure as shown in Fig. 12, that is, an antiparallel vortex pair produces strong strain regions near the hyperbolic stagnation points between themselves. The formation of such strong strain regions by antiparallel pairs provides a key to understand the physical mechanism of strong stretching of material lines. Before discussing how antiparallel pairs produce strong stretching, it may be important to mention that each tubular vortex has a much longer lifetime compared with the Kolmogorov time, which is the typical time scale of material line deformation (see Section 3.2). It is therefore meaningful to investigate the stretching process as a dynamical role of the tubular vortices. In the following two subsections, the enhancement mechanism of material line stretching will be illustrated from both the two-dimensional viewpoint as in Fig. 12 and the three-dimensional viewpoint as in Fig. 10.

5.1. Cross-section of vortex pair

The easiest way to understand how tubular vortices enhance material line stretching is to observe stretching of material lines near the cross-section of a vortex because the cross-sectional flow structure has remarkable features as seen in Section 4.3. For this purpose, we perform DNS of motion of a set of infinitesimal material line elements, which are initially distributed homogeneously and as densely as the numerical grid points in the whole space. The homogeneity survives forever since the fluid is incompressible. This property is convenient to study qualitatively in which part of the fluid the local stretching rate becomes larger, although, as was stated in Section 2, DNS of infinitesimal material elements is not necessarily appropriate to obtain accurate statistics of material objects of finite size.

We plot in Fig. 14(a) the projections of material line elements, which are lengthened for visualization to be the same length, onto the cross-section shown in Fig. 12. Only material line elements located near, within five numerical grids ($\approx 3\eta$), the cross-section are plotted. They are coloured

according to their stretching rate with red for stronger stretching. Fig. 14(b) shows contours of the magnitude of stretching rate of material line elements. It is clearly seen that strong stretching of material line elements does take place around the strong strain regions seen in Fig. 12(d). The velocity field relative to the centre of the figure is also plotted in Fig. 14(b) for convenience. The local stretching rate, as the strain rate in Fig. 12(d), takes larger values around hyperbolic stagnation points on the cross-section, while it is small around elliptic stagnation points. Of course, the latter type of stagnation points are located near the centres of tubular vortices.

In order to understand strong stretching around hyperbolic stagnation points, we observe the direction of the projections of strongly stretched material line elements, i.e., red ones. First, they have almost same and relatively long lengths, implying that they are nearly parallel to the cross-section. Second, they are approximately parallel to the extending direction emanating from each hyperbolic stagnation point on the cross-section. This alignment obviously yields effective stretching there because the direction is nearly parallel to the eigenvector of the rate-of-strain tensor associated with the largest positive eigenvalue (see Fig. 13). It is likely that around hyperbolic stagnation points the material lines tend to align with the eigenvectors, since streamlines are nearly parallel to the eigenvectors in such regions. Note again that the strong strain field takes place near hyperbolic stagnation points. Thus, material lines are stretched intensively around the hyperbolic stagnation points as seen in Fig. 14(b), and strong stretched line elements take a T-shaped form between the antiparallel vortices (Fig. 14(a)). Although the alignment between material lines and eigenvectors of the rate-of-strain tensor for the whole domain discussed in Section 3.4 is not simple, the alignment seems to be fairly simple as long as we observe them near a vortex pair on their cross-section. This tendency of simple alignment of strongly stretched parts of material lines will be clearly seen in three-dimensional visualization in the next subsection.

5.2. Three-dimensional flow field

It is not difficult to confirm stretching enhancement by antiparallel vortex pairs in three-dimensional visualizations. We may observe in Fig. 15 that strong stretching regions of material line elements, indicated by blue blobs, are located between the antiparallel pairs of tubular vortices. The vortex clusters in Fig. 15(a) and antiparallel pairs in Fig. 15(b) are respectively identical to those shown in Figs. 10(a) and (b). The stretching of material lines is indeed enhanced by antiparallel pairs of vortices as readily expected from the discussion in the preceding subsection.

Deformed material lines are too complicated if we observe them on the energy-containing scales as shown in Fig. 1. However, it is relatively simple and independent of the Reynolds number if we look at them on the Kolmogorov scales (Fig. 2). This is because the material line deformations are mainly governed by the tubular vortical structures, and they have Reynolds-number independent structure in the Kolmogorov scale as seen in Figs. 10(b) and (d). Material lines deformed by turbulence at $R_\lambda = 84$ are plotted in Fig. 16 together with the cluster of tubular vortices shown in Fig. 10(b). Only the material lines near the central vortex are plotted. The lines are coloured according to the local stretching rate γ_e , that is, white parts are more intensively stretched, $\gamma_e \geq \langle \gamma_e \rangle + (\langle \gamma_e^2 \rangle - \langle \gamma_e \rangle^2)^{1/2}$. At first glance, the deformed lines are still too complicated; however, careful observation leads us to a simple conclusion as described below. Figs. 16(a) and (b) are respectively the bottom and the side views of the cluster of antiparallel vortices shown in Fig. 10(b). Here, recall the discussion of the stretching enhancement on a cross-section of a tubular vortex. The strongly stretched material lines

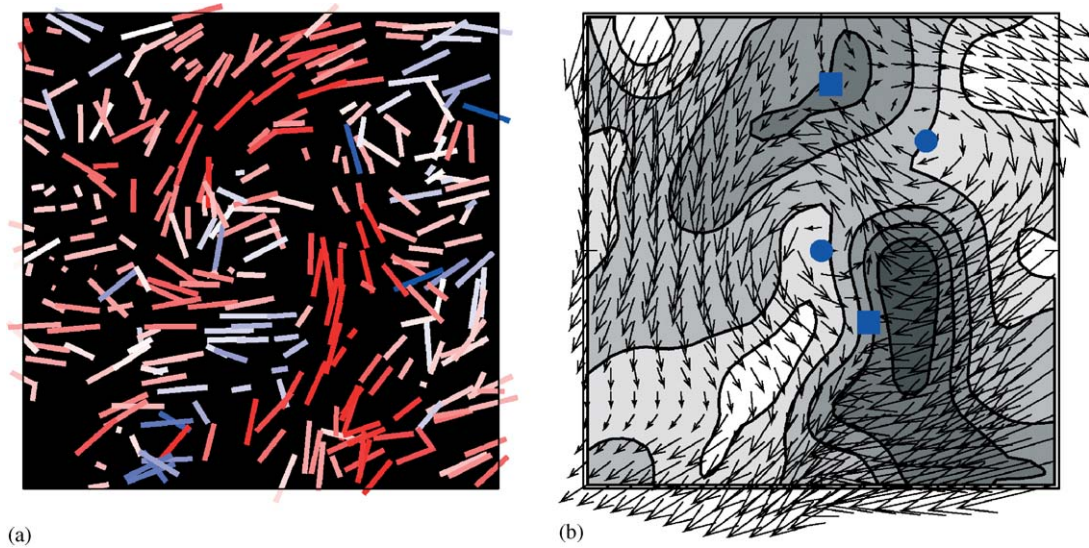


Fig. 14. Stretching of material line elements near (within 3η) the cross-section shown in Fig. 12. (a) Projection of line elements of the same length. Colour of line indicates the strength of local stretching rate with red for stronger stretching and blue for weaker. (b) Magnitude of local stretching rate of line elements. Contour levels are $0.1n\tau_\eta^{-1}$ ($n = 0, \dots, 4$). Stronger regions are shaded. The velocity field, which is identical to Fig. 12(c), is plotted with arrows. Solid circles denote elliptic stagnation points, and solid squares denote hyperbolic ones.

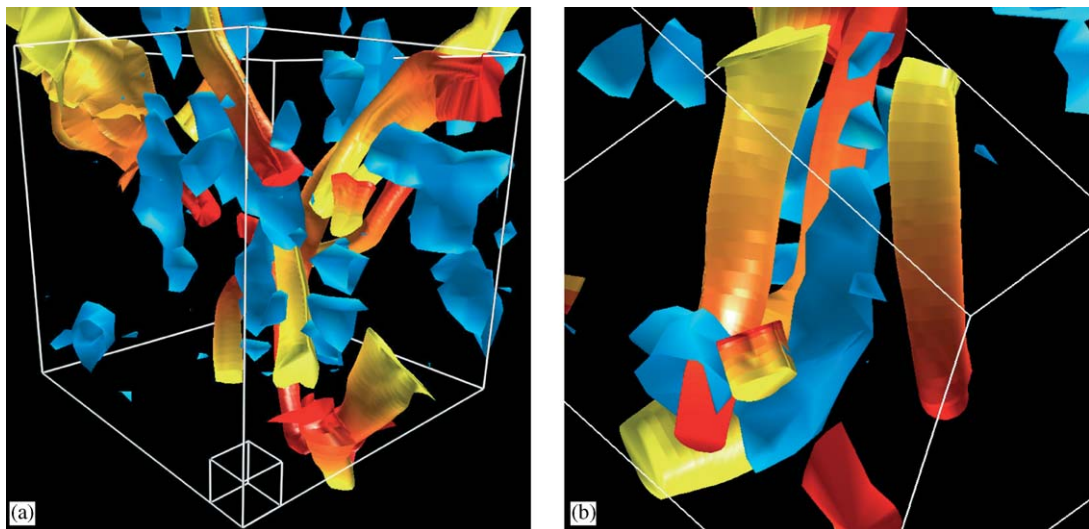


Fig. 15. Stretching enhancement by vortex clustering. Iso-surface (threshold being $0.36\tau_\eta^{-1}$) of stretching rate of material line elements are drawn by blue blobs together with (a) the tubular vortex cluster shown in Fig. 10(a), and (b) the antiparallel vortex pairs shown in Fig. 10(b). The latter is a magnification of the former.

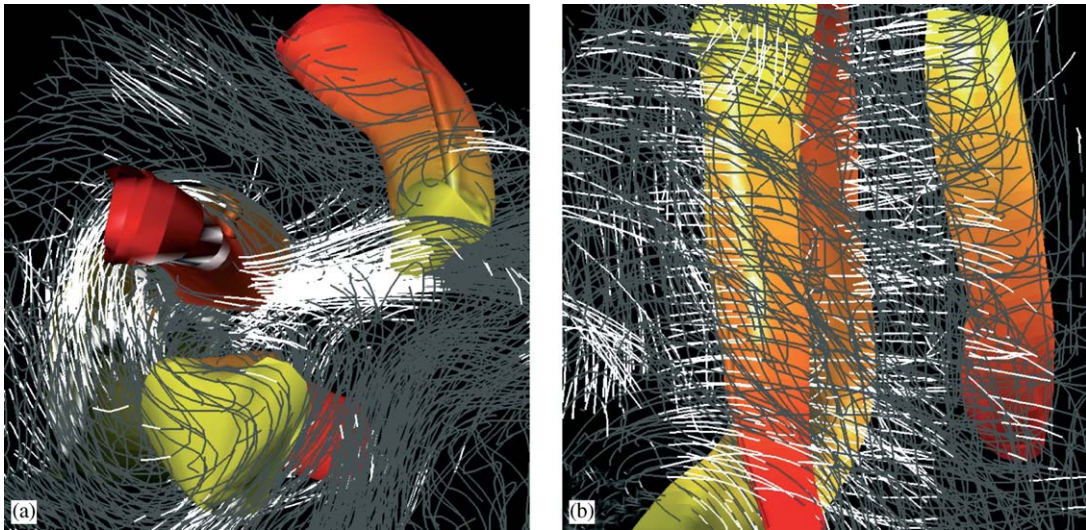


Fig. 16. Stretching enhancement by a vortex cluster. Deformed material lines are plotted together with the vortex cluster shown in Fig. 10(b) from two different viewpoints. (a) Bottom view and (b) side view, the latter of which is seen from almost the same angle as in Fig. 10(b). On white parts of the material lines, the local stretching rates γ_e are larger than a threshold, the average of γ_e plus its standard deviation.

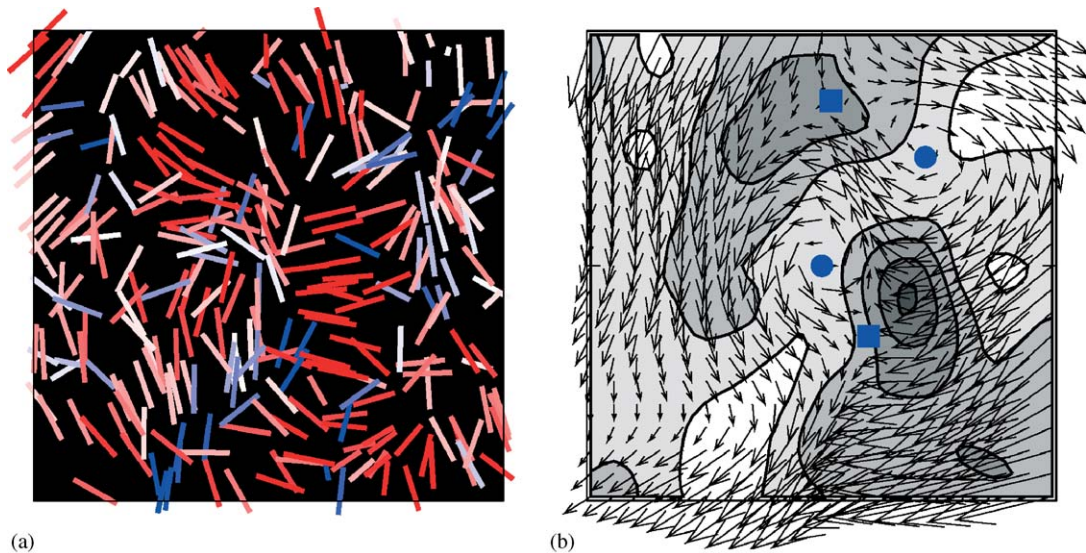


Fig. 17. Stretching of material surface elements near the cross-section shown in Fig. 12. (a) Projection of normal vectors of surface elements. Colour indicates the strength of local stretching rate with red for stronger stretching and blue for weaker. (b) Magnitude of local stretching rate of surface elements. Contour levels are $0.2n\tau_\eta^{-1}$ ($n = 0, \dots, 4$). Arrows denote the velocity vectors, which are identical to Fig. 12(c). Solid squares and circles are the hyperbolic and elliptic stagnation points, respectively.

Table 4

Volume fraction and mean stretching rate of material lines in each region which is concerned with j tubular vortices. Average over 20 realizations of turbulence at $R_\lambda = 84$

Regions	Fraction (%)	Stretching rate
Inside	24	$0.14\tau_\eta^{-1}$
$j = 0$	4	$0.16\tau_\eta^{-1}$
$j = 1$	16	$0.18\tau_\eta^{-1}$
$j = 2$	19	$0.20\tau_\eta^{-1}$
$j = 3$	16	$0.22\tau_\eta^{-1}$
$j = 4$	10	$0.23\tau_\eta^{-1}$
$j \geq 5$	10	$0.26\tau_\eta^{-1}$

should be located around hyperbolic stagnation points, and they take a T-shaped form. In Fig. 16(a), we see the behaviour of the stretching on the cross-section of the vortex cluster, where the central vortex induces clockwise swirling flow around it, and the other two vortices yield anti-clockwise ones. We may observe that two clusters of white material lines form a T-shape. The left vertical white cluster corresponds to the head of the T-shape of strong stretching parts of material lines associated with the central and bottom vortices, while the central horizontal white cluster can be regarded as not only its foot but also the head of another T-shape associated with the central and right vortices. It is clearly seen in Fig. 16(b) that almost all the white parts of the material lines exist parallel to each other and perpendicular to the vortices. In other words, the strong stretching can be regarded as a two-dimensional phenomenon. Hence, this feature justifies the argument that stretching enhancement takes place on cross-sections of tubular vortices as was done in the preceding subsection. These observations are completely consistent with the conclusion obtained there that the stretching is enhanced in strong strain regions near the hyperbolic stagnation points.

A comment may be in order here on the negative correlation between the local curvature and the local stretching rate of material lines seen in Fig. 8. As mentioned in Section 4.1 (see Fig. 10) the tubular vortices have the radius of $O(5\eta)$. On the other hand, the peak of the PDF of local curvature is around $\alpha_e \approx 0.05\eta^{-1}$ (Fig. 6), that is, the corresponding radius of curvature is about 20η . These are consistent with the picture observed in Fig. 16, namely the material lines are stretched by vortex clusters rather than single vortices. Of course, there are fractions of material lines which are wrapped by a single vortex, and their radii of curvature are around 5η , but they have only small stretching rates. On the other hand, the white parts seen in Fig. 16 have obviously smaller curvatures than such parts wrapped by single vortices. This is a physical explanation of the negative correlation between the local curvature and the local stretching rate.

Finally, we refer to a quantitative estimation which supports the stretching enhancement by clusters of the tubular vortices. For this purpose, we divide the whole space outside of vortex cores into regions according to the number of tubular vortices which affect it. Here, we define the domain affected by a vortex as a tubular region whose local radius is c ($=3$, say) times as long as the core radius of the vortex. We list the volume fraction of such parts in Table 4, together with the mean stretching rate of material lines in each region. In this estimation we neglect vortices shorter than a threshold, 10η . If we take all the identified vortices into account, the volume fraction inside their

cores is about 30% (Makihara and Kida, 2003). In this table, the value of j denotes the number of vortices which affect the region. It is clear that the larger the number is, the stronger the stretching rate becomes. This implies that tubular vortices enhance the stretching by forming clusters. It may be speculated that antiparallel pairs, which are most probable in a cluster as seen in Fig. 11, play key roles in the stretching, although further quantitative investigations are necessary to draw a final conclusion.

6. Concluding remarks

The physical mechanism of the intensive stretching of material lines in turbulence is investigated by the use of DNS. Deformations of material lines by homogeneous isotropic turbulence are statistically characterized by Kolmogorov scale variables. The average stretching rate of material lines is $0.17\tau_\eta^{-1}$ and the average curvature is $0.1\eta^{-1}$ irrespective of the Reynolds number. In this sense, the deformations are mainly governed by fluid motions on the Kolmogorov scale, i.e., the smallest scale of the Lagrangian motions in turbulence. On the other hand, it is clearly seen, by a highly objective identification method of coherent structures on the small scales, that there exist coherent vortical structures with tubular shape, which tend to align to each other in an antiparallel manner. Note that cross-sectional structures of tubular vortices seem to be characterized by the Kolmogorov variables, while their longitudinal length varies between the Kolmogorov length and the integral length. We have stressed that the cross-sectional flow of a cluster of vortices whose axes almost align with each other plays key roles in the effective stretching of material lines. More precisely, an antiparallel vortex pair always produces a flow accompanied with both two hyperbolic stagnation points on the cross-section and a strong strain region near the stagnation points. Since material lines tend to align to the eigenvector associated with the largest positive eigenvalue around the hyperbolic stagnation points, the stretching rate of material lines takes large values there. The directions of the eigenvectors corresponding to the positive eigenvalues around the two hyperbolic stagnation points take a T-shaped form, and therefore strongly stretching parts of material lines are observed with a T-shape between an antiparallel vortex pair. It should be stressed here that a single vortex does not possess the ability to stretch a material line strongly. A simple wrapping of a material line around a single vortex leads to algebraic stretching after a sufficiently long time. It seems that wrapping by a pair of antiparallel vortices keeps exponential stretching forever around the hyperbolic stagnation points.

The stretching of material lines is closely related to that of material surfaces because a material surface can be regarded as a set of material lines. Deformation of material surfaces in turbulence is of special interest, and has been intensively investigated as a foundation of turbulent mixing, since a material surface is merely the boundary between two parts of a fluid. So far in the present article, we have restricted ourselves within the stretching of material lines. Here, we describe briefly the case of material surfaces. In Fig. 17, we plot the projections of normal vectors and the contour of local stretching rate of material surface elements on the same cross-section shown in Fig. 14. Colours of the projections indicate the stretching rate of the elements. The strong stretching regions of material surfaces are also located around hyperbolic stagnation points denoted by solid squares in Fig. 17(b), similarly to the case of the material lines. It is also interesting to see that the normal vectors of strongly stretched material surface elements, i.e., red projections, are nearly

perpendicular to the expanding direction around the two hyperbolic stagnation points. Hence, the stretching of material surfaces is enhanced in the region around the hyperbolic stagnation points due both to the strong strain and to the alignment of the elements to eigenvectors of the rate-of-strain tensor. Since the effective extension of the boundary of two parts of fluid leads to strong mixing, we expect turbulent mixing on small scales to be enhanced by the antiparallel pairs of tubular vortices.

Finally, we discuss again the validity of Kolmogorov's similarity law in the statistics of material objects. It has been shown numerically in Section 3 that the average stretching rate and the average curvature of material lines of finite length are excellently scaled with the reciprocals of the Kolmogorov time and the Kolmogorov length, respectively, irrespective of the Reynolds numbers ranging between $R_\lambda = 57$ and 252. We notice however that the present estimation is made for a set of material lines which are artificially chopped at every numerical time step to have an approximately constant length of $O(\mathcal{L})$. Since the average curvature is $O(0.1/\eta)$ irrespective of the Reynolds number, the gyration radius of the chopped material lines becomes smaller compared with the energy-containing-scale length \mathcal{L} for larger Reynolds numbers. It may be possible that the statistics of material lines which are infinitely long, or long enough to have gyration radii as large as \mathcal{L} , are quantitatively and/or qualitatively different from those dealt with here. It is likely that such a difference, if any, is small, at relatively small Reynolds numbers, $R_\lambda = O(10)$ say, but becomes non-trivial at larger R_λ where the length scales, \mathcal{L} and $\eta(\propto R_\lambda^{-3/2}\mathcal{L})$, are sufficiently separated. In other words, the statistics of infinitely long material lines may suffer a mixing transition around $R_\lambda = O(100)$ (Dimotakis, 2000). In this sense, although the validity of Kolmogorov's similarity law in the statistics of chopped material lines of $O(\mathcal{L})$ has been clearly confirmed, that for infinitely long material lines has not been done yet and is left for a study in the near future.

Acknowledgements

The authors thank Dr. T. Makihara for his assistance in DNS data analysis. This work has been partially supported by a Grant-in-Aid for Scientific Research on Priority Areas (B) from the Ministry of Education, Culture, Sports, Science and Technology of Japan.

References

- Batchelor, G.K., 1952. The effect of homogeneous turbulence on material lines and surfaces. *Proc. R. Soc. London A* 213, 349–366.
- Batchelor, G.K., Townsend, A.A., 1956. Turbulent diffusion. In: Batchelor, G.K., Davies, R.M. (Eds.), *Surveys in Mechanics*. Cambridge University Press, Cambridge, pp. 352–399.
- Dimotakis, P.E., 2000. The mixing transition in turbulent flows. *J. Fluid Mech.* 409, 69–98.
- Drummond, I.T., Münch, W., 1991. Distortion of line and surface elements in model turbulent flows. *J. Fluid Mech.* 225, 529–543.
- Girimaji, S.S., Pope, S.B., 1990. Material–element deformation in isotropic turbulence. *J. Fluid Mech.* 220, 427–458.
- Goto, S., Kida, S., 2002. Multiplicative process of material line stretching by turbulence. *J. Turbulence* 3, 017.
- Kida, S., Goto, S., 2002. Line statistics: stretching rate of passive lines in turbulence. *Phys. Fluids* 14, 352–361.
- Kida, S., Miura, H., 1998a. Identification and analysis of vortical structures. *Eur. J. Mech. B/Fluids* 17, 471–488.

- Kida, S., Miura, H., 1998b. Swirl condition in low-pressure vortex. *J. Phys. Soc. Jpn.* 67, 2166–2169.
- Kida, S., Miura, H., 2000. Double spirals around a tubular vortex in turbulence. *J. Phys. Soc. Jpn.* 69, 3466–3467.
- Kida, S., Miura, H., Adachi, T., 2001. Flow structure visualization by low-pressure vortex. In: Vassilicos, J.C. (Ed.), *Intermittency in Turbulent Flows*, Vol. 69. Cambridge University Press, Cambridge, pp. 262–276.
- Kolmogorov, A.N., 1941. The local structure of turbulence in incompressible viscous fluid for very large Reynolds numbers. *Dokl. Akad. Nauk SSSR* 30, 301–305 (English translation in *Proc. R. Soc. London, Ser. A* 434, 9–13 (1991)).
- Makihara, T., Kida, S., 2003, in preparation.
- Makihara, T., Kida, S., Miura, H., 2002. Automatic tracking of low-pressure vortex. *J. Phys. Soc. Jpn.* 71, 1622–1625.
- Miura, H., Kida, S., 1997. Identification of tubular vortices in turbulence. *J. Phys. Soc. Jpn.* 66, 1331–1334.
- Siggia, E.D., 1985. Collapse and amplification of a vortex filament. *Phys. Fluids* 28, 794–805.